



## Technical Paper

## Multivariable control of ball-milled reactive material composition and structure

Matteo Aureli<sup>a,\*</sup>, Constantine C. Doumanidis<sup>b</sup>, Aseel Gamal Suliman Hussien<sup>c</sup>, Syed Murtaza Jaffar<sup>c</sup>, Nikolaos Kostoglou<sup>d</sup>, Yiliang Liao<sup>a</sup>, Claus Rebholz<sup>e</sup>, Charalabos C. Doumanidis<sup>f,g</sup>

<sup>a</sup> Mechanical Engineering Department, University of Nevada, Reno 1664 N. Virginia Street, Reno, NV 89557-0312, USA

<sup>b</sup> Department of Electrical and Computer Engineering, Aristotelian University of Thessaloniki, Greece

<sup>c</sup> Department of Mechanical Engineering, Khalifa University, Abu Dhabi, United Arab Emirates

<sup>d</sup> Department of Materials Science, Montanuniversität Leoben, Leoben, Austria

<sup>e</sup> Department of Mechanical & Manufacturing Engineering, University of Cyprus, Nicosia, Cyprus

<sup>f</sup> Office of the Provost, Nazarbayev University, Astana, Kazakhstan

<sup>g</sup> College of Engineering & Computer Science, Vin University, Hanoi, Viet Nam

## ARTICLE INFO

## Keywords

Ball milling  
Reactive multilayers  
Plastic deformation  
Diffusion penetration  
Multivariable control

## ABSTRACT

In reactive bimetallic compounds such as Ni–Al multilayers, desirable thermo-kinetic properties upon ignition require simultaneously controlled geometric microstructure and material composition. This article establishes fundamental dynamical models of plastic deformation and material diffusion in ball milling processing of particulates from Ni and Al powders, for the purpose of designing and implementing feedback control strategies for process control. The role of heat dissipation from plastic yield and friction slip in affecting compressibility and diffusivity of the material is elucidated. The different sensitivity of compressibility and diffusivity to thermal power is exploited by introducing multivariable control of both bilayer thickness and penetration depth simultaneously, using a real-time computational model as an observer with adaptation informed by infrared measurements of external vial temperature. The proposed control scheme is tested on a laboratory low-energy ball milling system and demonstrated to effectively modulate power intensity and process duration to obtain the desired microstructure and material composition.

## Nomenclature

$a$	diffusion area [m <sup>2</sup> ]
$A$	external vial surface [m <sup>2</sup> ]
$\mathbf{A}$	thermal state matrix
$b$	average bilayer size [m]
$b_d$	desired bilayer size [m]
$b_0$	initial bilayer size [m]
$b'$	size of specific bilayer [m]
$\mathbf{B}$	thermal input matrix
$\gamma$	shear strain [rad]
$c$	total heat capacity of vial content [J/K]
$c_i$	specific heat capacity of component $i$ in vial [J/kg K]
$C$	heat capacity of vial [J/K]
$\mathbf{C}$	thermal output matrix
$d$	average penetration depth of diffusion [m]
$d_d$	desired penetration depth [m]
$d_0$	initial penetration depth [m]
$\langle D \rangle$	mean free path of impactor [m]
$D$	diffusivity of Ni in Al [m <sup>2</sup> /s]

$D_0$	initial diffusivity of Ni [m <sup>2</sup> /s]
$D'$	diffusivity of Al in Ni [m <sup>2</sup> /s]
$Dt_b$	process duration for desired bilayer thickness [s]
$Dt_d$	process duration for desired diffusion depth [s]
$Dt_o$	process duration [s]
$\epsilon$	strain [m/m]
$\epsilon_y$	yield strain [m/m]
$e$	strain beyond yield [m/m]
$E$	Young's modulus [N/m <sup>2</sup> ]
$\mathbf{E}$	thermal error vector
$E_b$	bilayer size error [m]
$E_d$	penetration depth error [m]
$E_0$	error in pyrometric measurement of temperature [K]
$f$	collision frequency [Hz]
$g$	adaptation gain [1/K s]
$G$	shear modulus [N/m <sup>2</sup> ]
$G_i(s)$	internal thermal transfer function [K/J]
$G_o(s)$	external thermal transfer function [K/J]
$\eta$	mechanical efficiency [–]
$h$	heat transfer coefficient [W/m <sup>2</sup> K]

\* Corresponding author.

E-mail address: [maureli@unr.edu](mailto:maureli@unr.edu) (M. Aureli)

$H$	dissipated mechanical power [W]
$\theta$	thermal state vector
$\theta_d$	desired thermal state vector
$\theta_i$	internal over-temperature of vial [K]
$\theta_m$	average over-temperature of vial [K]
$\theta_o$	external over-temperature of vial [K]
$\mathcal{I}$	current [A]
$I$	identity matrix
$j$	sample number [-]
$k_1, k_2$	thermal controller gains [W/K]
$k_f$	friction gain [-]
$k_p$	plasticity gain [-]
$K$	compression rate gain [J <sup>-1</sup> ]
$\mathbf{K}$	thermal controller gain vector
$\mu$	friction coefficient [-]
$m$	mass of impactor-particulate pair [kg]
$m_i$	mass of component $i$ in vial [kg]
$m'$	mass of particulate [kg]
$M$	mass of impactor [kg]
$\nu$	Poisson ratio [-]
$n$	number of balls [-]
$N$	target number of sampling steps [-]
$P$	electrical power [W]
$P_{ave}$	average power value [W]
$P_{hi}$	high power value [W]
$P_{lo}$	low power value [W]
$P_0$	nominal power value [W]
$P_{max}$	maximum electric power [W]
$Q$	diffused mass [kg]
$Q_0$	activation energy [J/mol]
$\rho$	density [kg/m <sup>3</sup> ]
$r_i$	internal radius of vial [m]
$r_m$	effective radius of vial wall [m]
$r_o$	external radius of vial [m]
$r$	convective thermal resistance [K/W]
$R$	thermal resistance of vial [K/W]
$\mathcal{R}$	ideal gas constant [J/mol K]
$\sigma$	normal stress [N/m <sup>2</sup> ]
$\sigma_y$	yield stress [N/m <sup>2</sup> ]
$s$	Laplace variable [Hz]
$\tau$	shear stress [N/m <sup>2</sup> ]
$t_{sam}$	sampling period [s]
$\tau_s$	slip stress [N/m <sup>2</sup> ]
$t$	flight time of impactor [s]
$T_a$	ambient temperature [K]
$T_d$	desired temperature [K]
$T_i$	internal temperature to vial [K]
$T_m$	average temperature of vial [K]
$T_o$	external temperature of vial [K]
$T_o^*$	external temperature measured pyrometrically [K]
$v$	velocity of impactor [m/s]
$U$	average kinetic energy of impactor [J]
$U_i$	kinetic energy of impactor in $i$ degree of freedom [J]
$U_f$	dissipated friction energy [J]
$U_n$	kinetic energy of impactor in normal direction [J]
$U_p$	dissipated plastic energy [J]
$U_t$	kinetic energy of impactor in shear direction [J]
$U_y$	restored kinetic energy [J]
$v_i$	velocity of impactor in $i$ degree of freedom [m/s]
$V$	volume of particle [m <sup>3</sup> ]
$\mathcal{V}$	voltage [V]
$w$	volume of vial [m <sup>3</sup> ]
$W_e$	elastic volumetric work [J/m <sup>3</sup> ]
$W_f$	stored volumetric work [J/m <sup>3</sup> ]
$W_n$	volumetric work in normal h direction [J/m <sup>3</sup> ]
$W_p$	plastic volumetric work [J/m <sup>3</sup> ]

$\phi$	probability density function [-]
$\chi$	concentration of Ni [-]
$\chi_0$	initial concentration of Ni [-]
$x$	depth dimension [m]
$y$	thermal output vector
$z$	$\mathcal{Z}$ -transform variable [-]

## 1. Introduction

Over the past two decades, nanoscale layers of alternating reactive materials such as Ni–Al [1] and other bimetallic systems [2] have been integrated via mechanical alloying of elemental powders into composite particulates by ball milling (BM) [3]. These multilayer structures possess random fractal microstructural formations, see Fig. 1 [4], and yield spontaneous combustion synthesis of various intermetallic compounds, such as NiAl [5], when ignited thermally, electrically, or by mechanical impact [6]. This phenomenon is accompanied by impulsive and localized release of intense heat via self-propagating exothermic reactions (SPER). Thus, potential application of these energetic materials in microscale coating, sintering, soldering, welding, curing, etc., has motivated research for understanding and optimizing their layered structure in relation to their operational performance for a variety of self-heating devices and applications [7].

The thermal properties of such bimetallic nanomaterials, including ignition temperature, propagation velocity of the reaction front, exothermic enthalpy release, and adiabatic temperature obtained, have been studied experimentally and computationally, and shown to depend on structure scale [8]. The geometric aspects of multi-scale layered structures exhibit self-similar globular agglomerate and lamellar networks, see Fig. 1, and have been characterized by a fractal (Hausdorff) dimension [9]. It has been determined that longer BM processing times yield more refined structures with smaller bilayer size. These display a more extensive interfacial surface, associated with larger bimetallic boundary area and higher Gibbs free energy for reaction activation, which promote lower-temperature ignition and faster SPER propagation [8]. Larger size domains, on the contrary, dissipate and hamper conductive heat transfer, resulting in sluggish kinetics, occasionally even quenching the reaction and arresting its propagation [4].

On the other hand, the material composition aspects of multilayer structures, i.e. the bimetallic concentration fields, also determine

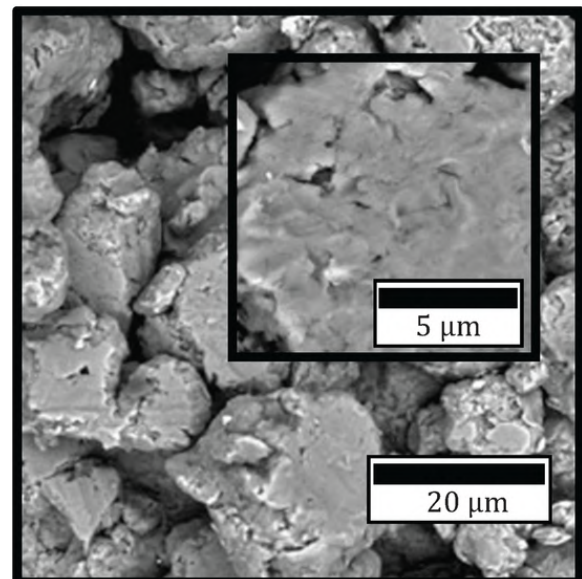


Fig. 1. Scanning electron micrograph of Ni–Al (1:1) particulate, after BM at 300 rpm for 13 h [4].

the diffusive mass transfer across their boundaries, thus significantly influencing the observed SPER thermodynamics. Prolonged BM processing of particulates results in overly fine nanolayers with high surface area/volume ratio and temperature gradients during BM, enhancing metal diffusion and alloying [3]. These, in turn, result into regions of solid solution and/or premature formation of intermetallics such as  $\text{NiAl}_3$ . The concomitant undesirable enthalpy release during fabrication reduces reaction potentials, exothermic heat, and adiabatic temperatures upon successive ignition [4].

It is thus clear that careful control of the BM process and the resulting thermal exposure of the particulates is essential to obtain a desired geometric and compositional material structure, which in turn determines the kinetics and thermodynamics of the product properties and its thermal performance. Aside from system-level control based on predictive models of BM grinding circuits presented in the literature [10,11], early works have addressed composition regulation in carbide synthesis by BM [12]. Recently, our group has demonstrated separately adaptive control of the fractal dimension [13] and diffusion saturation [14] via thermal regulation in bimetallic BM particulate microstructures. However, optimizing the thermo-kinetic ignition properties of reactive materials requires simultaneous control of both structure geometry and material composition during the process [14]. So far, this problem has not been tackled in the literature. For this reason, the aim of the present paper is to fill this knowledge gap by introducing and validating modeling and control systems for holistic structural regulation of BM particulates. For the first time, this strategy allows to simultaneously control both geometry and composition of bimetallic BM particulate microstructures towards optimized properties and performance.

The rest of the paper is organized as follows. Section 2 establishes the dynamic models that will be employed for control of bilayer size in fractal reactive formations. Section 3 describes a model for the temperature-regulated diffusion penetration depth. Section 4 proposes a multi-variable control system architecture based on a real-time computational model used as an observer and demonstrates its implementation on a laboratory BM system. Section 5 presents and discusses the experimental results of the experimental control setup. Finally, Section 6 summarizes the conclusions of this study and identifies directions for future research.

## 2. Modeling and control of bilayer thickness

### 2.1. Plastic deformation

The SPER thermo-kinetics in ignited BM particulates with fractal microstructure depend on the degree of structural refinement and complexity, typically described by a fractal dimension [9,14–16]. However, a metric more easily visualized and measured on optical/electron 2D section micrographs, such as for example the one shown in Fig. 1, is the distribution of monometallic domain thickness or “bilayer size”  $b'$ . This is defined as the minimum boundary-to-boundary linear dimension crossing the centroid of each original powder particle integrated in the particulate, see Fig. 2 for the nomenclature. In the rest of this paper, the average bilayer size  $b = \langle b' \rangle$  will be used. This parameter can be robustly determined experimentally by blob segmentation, via standard scale-independent image processing algorithms [17].

Bilayer thickness is the result of compressive plastic deformation of the initial powders by collision events of particulates with the impactors (that is, milling balls and vial walls) during the BM period. In this work, it is assumed that the initial particle size distribution and the kinetic energy distributions of the BM impactors are known. Thus, the objective of this section is: (1) to describe the dynamic evolution of the bilayer thickness as a function of the process conditions, that is, the BM power dissipated as heat; and (2) to propose a preliminary feedback control system for the average bilayer size  $b$ .

BM impactors have been experimentally shown in [18] to follow a Brownian-like kinematics, described by a probability density func-

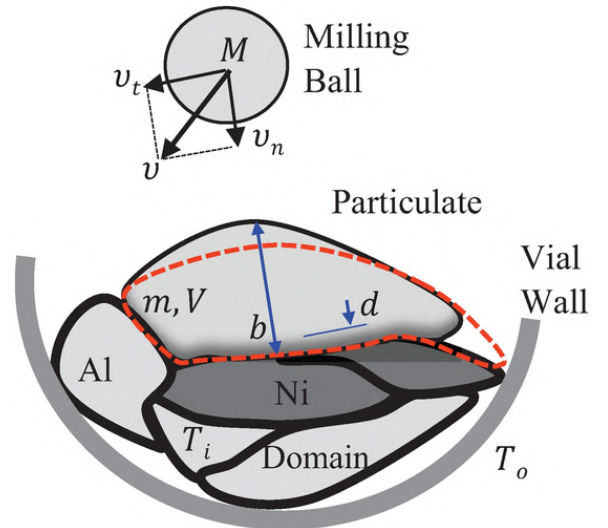


Fig. 2. Schematic arrangement of BM impactors and typical particulate (not to scale) along with relevant nomenclature. Upon impact, the particulate deforms to the red dashed line shape and the bilayer thickness  $b$  decreases. The shaded area in the particulate represents the penetration depth  $d$ , which increases over time due to diffusion.

tion (PDF) of the form

$$\phi(U_i) = \frac{2}{\sqrt{\pi}mv^2} \sqrt{\frac{U_i}{mv^2}} \exp\left(-\frac{U_i}{mv^2}\right) \quad (1)$$

where  $U_i$  is the kinetic energy associated to the impactor motion per degree of freedom  $i$  ( $i = 1, 2, 3$ ). In the PDF, the parameter  $v = \sqrt{\langle v_i^2 \rangle}$  is the root mean square (RMS) velocity in each direction of motion  $i$  and the average impactor kinetic energy is thus  $\langle U \rangle = (3/2)mv^2$ . The parameter  $v$  can be measured directly in the laboratory from video sequences of impactor motion. Alternatively, it can be determined indirectly via the steady-state average energy  $\langle U \rangle$  of the balls in the vial, which is in turn estimated from power measurements on the BM device during the transients to steady operation [18]. The equivalent mass  $m$  of the impactor-particulate pair is defined as the harmonic sum of their masses  $M$  and  $\langle m' \rangle$  respectively [19]. Specifically,  $m = M \langle m' \rangle / (M + \langle m' \rangle) \approx \langle m' \rangle$ , since typically  $M \gg \langle m' \rangle$  in BM. Thus,  $m$  can be determined from the statistics  $m'$  of the initial particle size distribution.

The individual material domains of a particulate compressed under an impact event, as schematically shown in Fig. 2, are assumed homogeneous and isotropic with elasto-plastic constitutive behavior with negligible strain-hardening, see Fig. 3a. In the stress-strain ( $\sigma, \epsilon$ ) diagram, after a linear elastic compression  $\sigma = E\epsilon$ , where  $E$  is the Young's modulus, the material deforms plastically at fixed yield stress  $\sigma_y$ . During the loading phase of a collision, the normal compressive component of the impactor kinetic energy  $U_n = U_i$  is absorbed as total volumetric work  $W_n = U_n/V$  over the volume  $V$  of the particle, corresponding to area OABC in Fig. 3a. Note that  $V$  is assumed known from the initial powder size statistics. During the unloading phase, that is, immediately after collision (or subsequently if residual stress fields are temporarily stored in the particle), elastic volumetric work  $W_e$  corresponding to area BCD  $\approx$  OAF is returned as kinetic energy  $U_y = W_e V$  back to the impactor-particulate content of the BM vial. The plastic volumetric work  $W_p$  (area OABD in Fig. 3a) is dissipated as thermal energy  $U_p = W_p V = U_n - U_y$ , where  $U_p = \max[U_n - U_y, 0]$  since  $U_i = U_n$ , with  $U_y = [\sigma_y^2 / (2E)]V$ . It is important to note here the dependence of  $U_p$  and  $U_y$  on the internal temperature  $T_i$  of the BM vial contents through the material properties  $E$  and  $\sigma_y$ . Also, the nonlinear relation of  $U_p$  on  $U_n$  can be approximately linearized as

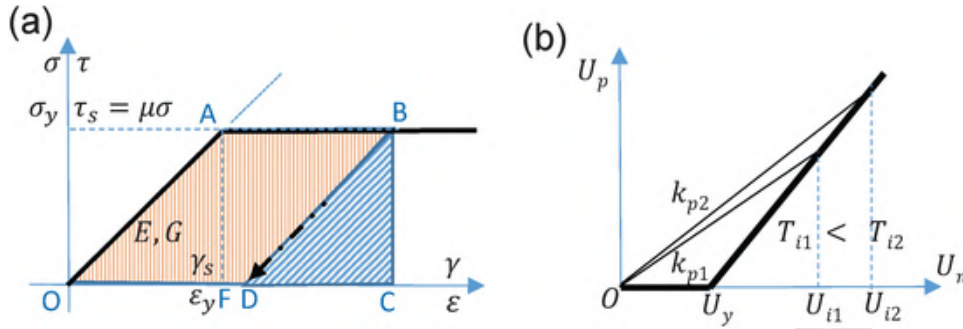


Fig. 3. (a) Constitutive material stress-strain model. (b) Approximate linearization and equivalent plastic deformation gain  $k_p = U_p/U_i$  for two levels of  $T_i$ .

$$U_p \approx k_p U_i \quad (2)$$

with a temperature-dependent plasticity gain  $k_p = U_p/U_i$  ranging from 0 when  $U_i < U_y$ , to 1 when  $U_i \gg U_y$ . The approximate linearization is displayed in Fig. 3b for two arbitrary values of  $T_i$ . Thus, this process leads to a PDF for  $U_p$  stemming from the one for  $U_i$  in Eq. (1).

## 2.2. Surface friction

In addition to plastic work, heat dissipation also occurs during collision because of friction slip on the contact surface normal to the compression direction [16], see Fig. 2. In the shear stress–strain ( $\tau, \gamma$ ) diagram in Fig. 3a, after a linear deformation  $\tau = G\gamma$  at shear modulus  $G$ , slip occurs at shear stress  $\tau_s = \mu\sigma$ , where  $\mu$  is the Coulomb dry friction coefficient. Note that  $G = E/[2(1 + \nu)]$ , where  $\nu$  is Poisson's ratio of the domain material. Upon impact, part of the kinetic energy  $U_i = 2U_y$  associated to the two degrees of freedom in the tangential direction to the surface, is initially stored in the material as volumetric work  $W_f$  (area OAF in Fig. 3a). It is subsequently released as friction energy  $U_f = W_f V$  upon unloading (area BCD). During elastic impact, the energy is assumed to be uniformly absorbed in stress fields over the domain volume  $V$  as

$$U_n = \frac{\sigma^2}{2E} V \quad \text{and} \quad U_f = \frac{\tau_s^2}{2G} V \quad (3)$$

This yields the friction energy as  $U_f = \min[2(1 + \nu)\mu^2 U_n, U_i]$ , which can be approximately linearized as

$$U_f \approx 2k_f U_i \quad (4)$$

where the friction gain  $k_f$  ranges from  $(1 + \nu)\mu^2$  to 1.

During steady-state operation in BM, the kinetic energy distribution of the impactors reported in Eq. (1) is preserved unchanged. Therefore, the entire mechanical energy introduced to the BM containers is converted into heat by plastic deformation and surface friction. Specifically, from Eqs. (2) and (4),

$$H = f(U_p + U_f) \approx f(k_p + 2k_f)U_i \quad (5)$$

where  $H$  is the mechanical power converted into thermal power, and  $f$  is the collision frequency. The converted mechanical power  $H$  can be estimated as  $H = \eta P$  from the BM device electrical power  $P = \mathcal{V}\mathcal{I}$ , with  $\mathcal{V}$  the voltage and  $\mathcal{I}$  the current of its servomotors, through an efficiency factor  $\eta$  accounting for aerodynamic resistance and transmission power loss. Similarly, the collision frequency  $f$  can be estimated for a vial of volume  $w$  with  $n$  balls translating at RMS velocity  $v$  per degree of freedom described by Eq. (1) as

$$f = \frac{n}{\langle t \rangle} \quad (6)$$

where  $\langle t \rangle$  is the average flight duration of a single impactor be-

tween successive collisions across a mean free path  $\langle D \rangle$ , see [18], so that  $\langle t \rangle = \langle D \rangle / v$  and  $\langle D \rangle = \sqrt[3]{w/n}$ .

## 2.3. Dynamic evolution of the bilayer thickness

The fraction of BM power  $P$  dissipated via plastic deformation  $fU_p$  is responsible for the useful gradual compressive strain of the particulate domains. This is defined as  $e = \varepsilon - \varepsilon_y$  and corresponds to the length  $AB = OD$  in Fig. 3a. Deformation occurs at yield stress  $\sigma_y = E\varepsilon_y$  across the particulate domains thickness according to  $fU_p \approx (k_p \eta P) / (k_p + 2k_f) = f\sigma_y e V$  so that

$$\dot{e} = f e \approx \frac{k_p}{k_p + 2k_f} \frac{\eta}{\sigma_y V} P = KP \quad (7)$$

where  $K$  can thus be defined as a compression rate gain. As exemplified in Fig. 2, the plastic compressive strain  $e$  is related to progressive differential reduction of the average bilayer size  $b$  as  $de = -(db)/b$ . Therefore, the plastic deformation dynamics can be described by a nonlinear state equation for the average bilayer thickness  $b$  which relates its rate dependence on BM input power  $P$  as

$$\begin{cases} \dot{e} = -\dot{b}/b \Rightarrow e = \ln(b_0/b) \Rightarrow b = b_0 \exp(-e) \\ \dot{b} = -b\dot{e} = -K b P \end{cases} \quad (8)$$

The value of gain  $K$  can be experimentally identified by linear interpolation as the slope of laboratory data on the  $(P, \dot{e})$  plane, see Eq. (7). The values of  $\dot{e} = -\dot{b}/b \approx -\Delta b/b \Delta t$  can be estimated from differential measurements of  $\Delta b$  on successive micrographs of particulate sections over BM time intervals  $\Delta t$ . Fig. 4 shows an example of estimation of the gain  $K$  from literature data [4,13,18] and laboratory measurements, as elaborated in Section 4. It appears that the value of  $K$  (aver-

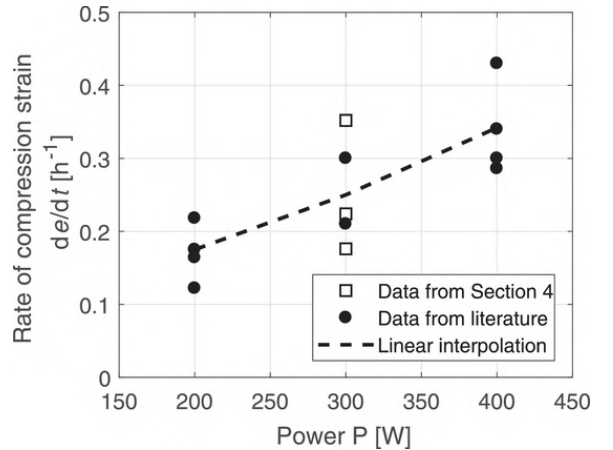


Fig. 4. Estimation of compressibility gain  $K$  from experimental data. Data from the literature are obtained from Refs. [4,13,18].

aging  $0.235 \times 10^{-6} \text{ J}^{-1}$  for the BM conditions described below) increases with  $P$  (+12% within 200–400 W). From Eq. (7), this phenomenon can be likely attributed to impactor energetics (due to increase of  $k_p$ , see also Fig. 3b) and, mainly, to material softening (reduction of yield point  $\sigma_y$ ) due to the elevated internal temperatures  $T_i$  in the container at higher power levels.

#### 2.4. Preliminary controller for the bilayer thickness

If in-process estimates of  $b$  are available as one BM output, a closed-loop control scheme could be realized to bring  $b$  to a desired bilayer size  $b_d$ , using real-time feedback of the bilayer size error  $E_b = b - b_d$ . Fig. 5 illustrates a possible implementation of such a feedback controller. Here, the controller is implemented in discrete time (where  $z$  denotes the variable for the  $\mathcal{Z}$ -transform, and  $j$  indicates the sample number) with sampling period  $t_{\text{sam}}$ . The goal is to bring the bilayer size error  $E_b$  to 0 within  $N$  sampling steps [20], by modulating the BM power  $P$  between 0 and a saturation limit  $P_{\text{max}}$ . Thus, letting  $\dot{b} \approx (b_d - b)/(Nt_{\text{sam}})$  and from Eq. (8), the power input at time step  $j$  is modulated as

$$P(j) = \text{sat} \left[ \frac{1}{KNt_{\text{sam}}} \frac{E_b(j)}{b(j)} \right]^{P_{\text{max}}} \quad (9)$$

where  $\text{sat}[\cdot]$  indicates saturation between the indicated lower and upper limits 0 and  $P_{\text{max}}$ .

The control law of Eq. hyperlinkeq:9(9) with  $N = 1$  steps, sampling time  $t_{\text{sam}} = 5$  min, and power saturation  $P_{\text{max}} = 300$  or 400 W is tested in simulation. Results are shown in Fig. 6. In the simulation, the regulator is set to bring the bilayer thickness from an initial  $b_0 = 40 \mu\text{m}$  to a specified  $b_d = 2 \mu\text{m}$ . Fig. 6a illustrates the power profile for two  $P_{\text{max}}$  levels (300 and 400 W), while Fig. 6b shows the respective transients of average bilayer size  $b$ . Upon starting, the controller immediately saturates (bang-bang) the power  $P$  at  $P_{\text{max}}$ , maintaining its value steady nearly throughout the process, while the bilayer thickness  $b$  drops from  $b_0$ . When the bilayer size reaches  $b_d$ , the error  $E_b = 0$

causes the power to shutdown at  $P = 0$ , as in Eq. (9). Note that this control law regulates plastic deformation by modulating the process duration, rather than adjusting its intensity. Fig. 6a and b show that the BM process takes approximately 12 h for  $P_{\text{max}} = 300$  W, while it only takes approximately 9 h for  $P_{\text{max}} = 400$  W to provide the same amount of plastic deformation work needed for the same specified bilayer size  $b_d$  (approximately 3600 W h). Note that, for a fixed power level  $P$ , the time  $Dt_{b0}$  needed to descend from bilayer thickness  $b_0$  to the specified  $b_d$  can be estimated from the exponential transient of Eq. (8) as

$$Dt_{b0} = \frac{1}{KP} \ln(b_0/b_d) \quad (10)$$

where  $K$  is assumed constant throughout the BM process, see also Fig. 6(b).

### 3. Modeling and control of diffusion penetration

#### 3.1. Thermal regulation

Process temperature significantly affects the dynamics of plastic deformation through changes in the gain  $K$  in Eq. (7), as well as through changes of bimetallic diffusivity [14]. Thus, it is necessary that the heat transfer process in the BM vial be modeled and regulated. The problem is schematically described in Fig. 7 which details the relevant nomenclature.

Thermal power  $H = \eta P$ , see Eq. (5), is released by plastic deformation and surface friction to the BM contents. The total heat capacity of the BM contents is estimated as  $c = \sum_i m_i c_i$ , determined by the rule of mixtures from the masses  $m_i$  and specific heat capacities  $c_i$  of each component  $i$  (e.g., stainless steel balls, Ni and Al powders). It is assumed that, through diffusion penetration control, no early reaction between the components and no exothermic enthalpy release take place during BM fabrication. Moreover, it is postulated that the BM contents are at a uniform temperature  $T_i$ . This assumption is justified by considering the effective mixing of the BM contents occurring upon im-

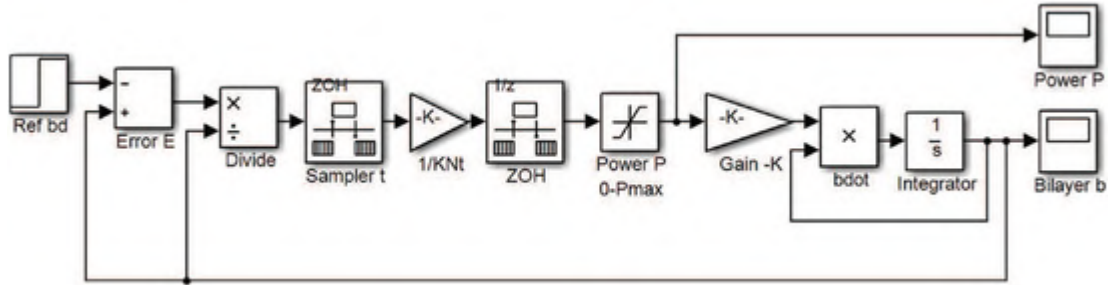


Fig. 5. Implementation of the discrete-time feedback controller for bilayer size. Note the saturation block to account for minimum and maximum available power.

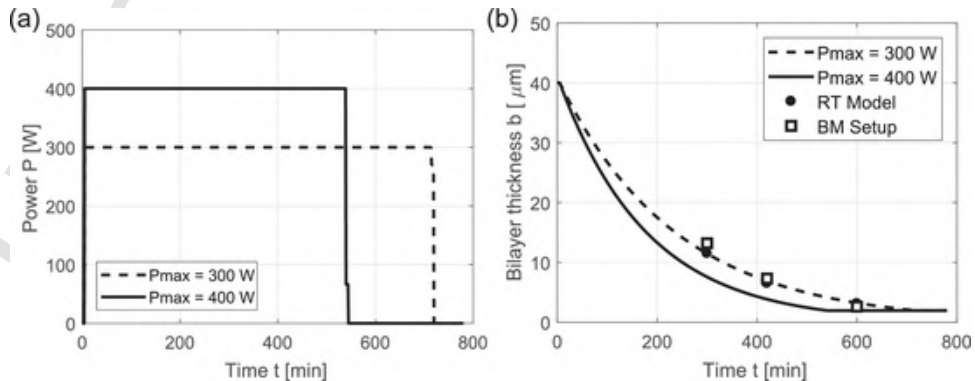


Fig. 6. Simulation results on plastic deformation (bilayer size) feedback control. (a) Input power profile  $P$ . (b) Evolution of bilayer size  $b$ . Details for the data labeled “RT Model” and “BM Setup” are in Section 4.

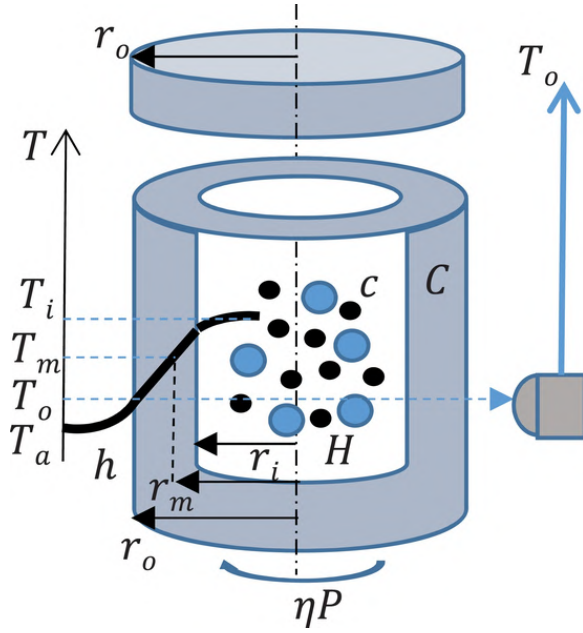


Fig. 7. Schematic arrangement of heat transfer in BM container (not to scale) and relevant nomenclature.

compact, efficient conductive heat transfer among metal species, and efficient radiation in the enclosed containers, so that the internal thermal distributions are equalized.

In addition, heat is further conducted through the container walls, that is, the vial cylindrical, bottom, and lid surfaces. These surfaces are made of homogeneous and isotropic material with total heat capacity  $C$  and thermal resistance  $R$ . The container is assumed at an average temperature  $T_m$  at the effective radius  $r_m$ . The effective radius is calculated as usual [14] as  $r_m = (r_o - r_i) / \ln(r_o/r_i)$  for cylindrical walls of internal and external radius  $r_i$  and  $r_o$ , respectively, see Fig. 7. The external surface  $A$  of the container at average temperature  $T_o$  radiates and convects heat to the surrounding inert gas at a constant ambient temperature  $T_a$ . This process is accounted for by considering a heat transfer coefficient  $h$  yielding a thermal resistance  $r = 1/(hA)$ . Thus, two thermal state equations are established by energy balances of the BM contents and container. By considering the power  $P$  to be the input to the system, defining as states the over-temperatures  $\theta_i = T_i - T_a$  and  $\theta_m = T_m - T_a$ , and as output  $\theta_o = T_o - T_a$ , which is measurable with an external infrared thermocouple, see Fig. 7, the thermal problem is described as

$$\begin{cases} c\dot{\theta}_i + (\theta_i - \theta_o)/R = \eta P \\ C\dot{\theta}_m + \theta_o/r = (\theta_i - \theta_o)/R \end{cases} \quad (11)$$

with  $\theta_m = (\theta_i + \theta_o)/2$ . Rearranging in matrix form,

$$\begin{bmatrix} \dot{\theta}_i \\ \dot{\theta}_m \end{bmatrix} = \begin{bmatrix} -2/cR & 2/cR \\ 2/CR & -2/CR - 2/C(R+2r) \end{bmatrix} \begin{bmatrix} \theta_i \\ \theta_m \end{bmatrix} + \begin{bmatrix} \eta/c \\ 0 \end{bmatrix} P \quad (12a)$$

$$\begin{bmatrix} \theta_i \\ \theta_o \end{bmatrix} = \begin{bmatrix} 1 & 0 \\ 0 & 2r/(R+2r) \end{bmatrix} \begin{bmatrix} \theta_i \\ \theta_m \end{bmatrix} \quad (12b)$$

or in compact state-space form with obvious meaning of the symbols  $\dot{\theta} = A\theta + BP$ ,  $y = C\theta$ . Here, the state vector is  $\theta = [\theta_i, \theta_m]^T$  and the output vector is  $y = [\theta_i, \theta_o]^T$ . The system can also be modeled as in [13] through the transfer functions  $G_i(s) = \Theta_i(s)/P(s)$  and  $G_o(s) = \Theta_o(s)/P(s)$ , where  $s$  indicates the Laplace variable. Specifically,  $G(s) = [G_i(s), G_o(s)]^T = C[sI - A]^{-1}B$ , see for example [20]. The para-

meters in Eq. (12) can be determined from the geometry, materials and kinematics of the BM setup. Specifically, for the laboratory device described in Section 4, it is found  $c = 217.5 \text{ J/K}$ ,  $C = 1305 \text{ J/K}$ ,  $R = 0.0203 \text{ K/W}$ ,  $r = 0.449 \text{ K/W}$ , and  $\eta = 0.84$ , see [14].

If real-time predictions of temperature states  $\theta$  are accessible, then a controller can be applied to regulate  $\theta$  to a desired value  $\theta_d$ . For example, a control law based on the state error vector  $E = \theta_d - \theta$  can be designed via pole placement for the closed-loop system [20] with full state feedback control gains  $k = [k_1, k_2]$ . That is, the input  $P$  is regulated as  $P = kE$  so that the characteristic equation  $\det[sI - (A - Bk)] = 0$  of the closed loop system reads

$$s^2 + \frac{4c(R+r) + C(R+2r)(2+\eta k_1 R)}{cCR(R+2r)}s + \frac{4 + 4\eta k_1(R+r) + 2\eta k_2(R+2r)}{cCR(R+2r)} = 0 \quad (13)$$

Selecting  $k_1 = 0$  and  $k_2 = k_2 r/(R+2r)$ , where  $k$  is a proportional gain, corresponds to output feedback control where  $P = k(T_d - T_o)$ . This control law is of practical interest because the external temperature  $T_o$  is accessible in real-time via infrared pyrometry sensing, see Fig. 7. As discussed in the next section, the reference temperature  $T_d$  of the inner-loop thermal regulator is to be modulated in-process, to provide the desired material diffusivity in order to control diffusion penetration, see also [14].

### 3.2. Penetration depth

Mutual inter-diffusion across the interface of bimetallic particulate domains results in bi-directional material flows, changing elemental concentrations in both sides. In BM of reactive material systems such as Ni-Al, such diffusion is often prominently asymmetric. Indeed, typical diffusivity of Ni atoms into the Al lattice is  $D = 3.4 \times 10^{-22} \text{ m}^2/\text{s}$ , with the reciprocal one being just  $D' = 3.6 \times 10^{-41} \text{ m}^2/\text{s}$  at BM internal temperatures  $T_i = 125 \text{ }^\circ\text{C}$  [21,22].

Therefore, material diffusion is of interest mainly for penetration of Ni into Al, across large-area, semi-planar interfacial surfaces between lamellar domains evolving during BM. Under such conditions, Fick's diffusion law yields the time-varying concentration  $\chi$  profile across the penetration direction  $x$  (normal to the boundary surface) over time  $t$ . Specifically, by letting  $\Delta\chi(x;t) = \chi(x;t) - \chi(0;t)$ , Fick's law reads see [14],

$$\begin{aligned} \Delta\chi(x;t) &= \Delta\chi_0 \left[ 1 - \frac{2}{\sqrt{\pi}} \int_0^{x/(2\sqrt{Dt})} \exp(-\tau^2) d\tau \right] \\ &= \Delta\chi_0 \text{erfc}(x/(2\sqrt{Dt})) \end{aligned} \quad (14)$$

where  $\text{erfc}(\cdot)$  indicates the complementary error function [23], and the interface concentration difference remains nearly fixed at  $\Delta\chi_0 = D/(D+D') \approx 1$  because of the asymmetry of diffusion.

A representative evolution of the time-varying concentration profile is displayed in Fig. 8. Each profile in Fig. 8 can be fully described by a lumped parameter  $d$  representing an average penetration depth. This depth is defined in correspondence to a fixed concentration increment  $\Delta\chi$  relative to  $\Delta\chi_0$  which, for convenience, is chosen as  $\Delta\chi(d;t)/\Delta\chi_0 = \text{erfc}(1) \approx 0.1573$ . This implies, then, for the definition of the average penetration depth

$$d(t) = 2\sqrt{Dt} \quad (15)$$

The average penetration depth  $d$  is also a convenient lumped descriptor of the cumulative mass  $Q$  of an element of density  $\rho$  diffused across surface area  $a$  of the interface. Specifically, from Eqs. (14) and (15),

$$Q(t) = a\rho \int_0^\infty \Delta\chi(x;t) dx = \frac{a\rho\Delta\chi_0}{\sqrt{\pi}} d(t) \quad (16)$$

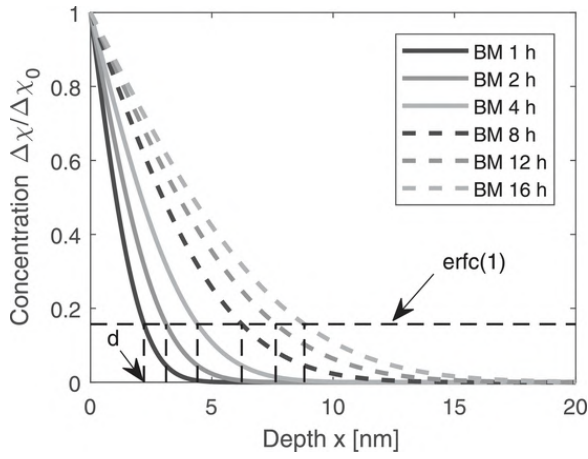


Fig. 8. Planar diffusion profiles of concentration distribution and penetration depth  $d$  of Ni in Al ( $T_i = 400$  K).

By differentiating Eq. (15) with respect to time, the dynamics of penetration depth  $d$  can be described as

$$\dot{d} = \frac{2D}{d} + \frac{d}{2D} \dot{D} \quad (17)$$

According to Arrhenius kinetics [14], the diffusivity  $D$  depends sensitively on the internal BM temperature  $T_i$  as

$$D = D_0 \exp\left(\frac{-Q_0}{\mathcal{R}T_i}\right) \quad (18a)$$

where  $D_0 = 0.292 \times 10^{-4} \text{ m}^2/\text{s}$  is the diffusion coefficient,  $Q_0 = 129.7 \text{ kJ/mol}$  the activation energy for Ni in Al, and  $\mathcal{R} = 8.314 \text{ J/mol K}$  is the ideal gas constant. By considering the time dependence of  $T_i$  in Eq. (18a), the time derivative of the diffusivity is thus

$$\dot{D} = \frac{DQ_0}{\mathcal{R}T_i^2} \dot{T}_i \quad (18b)$$

Eq. (18a) shows that, in BM processes, diffusion progresses predominantly at elevated steady-state temperatures. These temperatures are maintained largely constant during most of the process duration by the thermal regulator discussed above at the desired level  $T_d$ , so that  $\dot{T}_i \approx 0$ . Thus, for temperature-regulated BM, the diffusivity is largely constant, so that  $\dot{D} \approx 0$ . Thus, in Eq. (17), the second term is largely negligible during thermal steady-state. Therefore, the dominant nonlinear dynamics of penetration depth can be simplified as

$$\dot{d} \approx \frac{2D_0}{d} \exp\left(\frac{-Q_0}{\mathcal{R}T_i}\right) \quad (19)$$

where now the temperature  $T_i$  serves as the control input to penetration depth  $d$ .

### 3.3. Material diffusion control

If in-process estimates of average penetration depth  $d$  are feasible, a feedback control law similar to that developed for bilayer thickness in Eq. (5) could be implemented to regulate  $d$  to a specified reference depth  $d_d$ , using the error  $E_d = d_d - d$ . Assuming availability of the  $d$  signal, a controller can be designed by modulating the diffusivity  $D$  to bring the error  $E_d$  to zero in  $N$  sampling periods. In particular, following the derivation of Eq. (9) letting  $\dot{d} \approx (d_d - d)/(Nt_{\text{sam}})$  and from Eq. (19), the diffusivity input at time step  $j$  is defined as

$$D(j) = \text{sat} \left[ \frac{1}{2Nt_{\text{sam}}} d(j) E_d(j) \right]_{D(T_d)}^{D_0} \quad (20)$$

Thus, Eq. (20) regulates  $D(j)$  to a required value  $D_d(j)$ , subject to saturation between a minimal value  $D(T_a) = D_0 \exp(-Q_0/\mathcal{R}T_a)$  at ambient temperature  $T_a \approx 20^\circ\text{C}$  and  $D_0$ . This value  $D_d$  is, in turn, followed by modulation of the reference temperature  $T_d$  by the thermal regulator as, see Eq. (18a),

$$T_d(j) = \left(\frac{Q_0}{\mathcal{R}}\right) \ln \left[ \frac{D_0}{D_d(j)} \right] \quad (21)$$

Fig. 9 illustrates the structure of this outer-loop controller for the penetration depth implementing Eqs. (20) and (21) with inner-loop temperature regulation in Eq. (13). The architecture is tested in simulation on the temperature and diffusion dynamical models of Eqs. (12) and (19), respectively. The simulation is performed in discrete time with  $N = 1$  sampling period  $t_{\text{sam}} = 5$  min, enforcing BM power limits  $P_{\text{max}} = 300$  W and 400 W. Fig. 10a–d shows the responses of this control scheme for a penetration depth command  $d_d = 5$  nm, that is, 0.5% of bilayer thickness setpoint  $b_d$ , see Fig. 6b, for two-sided penetration.

For  $P_{\text{max}}$  set to 300 W, the control law product of  $d$  with  $E_d$  in Eq. (20) produces an excessive required diffusivity  $D_d$  (over  $3 \times 10^{-18} \text{ m}^2/\text{s}$ , see Fig. 10a), mandating high desired temperature  $T_d$  reaching  $250^\circ\text{C}$ , see Fig. 10c. However, the necessary power  $P$  saturates quickly at limit  $P_{\text{max}}$ , resulting into a lower temperature  $T_i$ , see Fig. 10c. This yields an actual diffusivity  $D$  from Eq. (18a) with s-shaped transient to lower than  $D_d$  values, resulting in gradual accumulation of penetration depth  $d$  to reach the targeted  $d_d$ . When  $d_d$  is eventually obtained, the diffusion controller in Eq. (20) drops  $D_d$  to the lowest value  $D(T_a)$ , that is,  $T_d$  is set to  $T_a$ , and the thermal controller shuts down power to  $P = 0$ . After a short cooling transient for the temperature  $T_i$ , see Fig. 10c, and an even faster decay for the diffusivity  $D$ , the eventual penetration  $d$  stabilizes to its final depth, see Fig. 10a.

When the maximum power limit  $P_{\text{max}}$  is raised from 300 to 400 W, the achievable temperature  $T_i$  rises from approximately 123 to  $154^\circ\text{C}$ , see Fig. 10c and d. This produces a dramatic increase in diffusivity  $D$  by nearly 20 times because of the sensitivity of Arrhenius kinetics on temperature, and penetration  $d$  rapidly exceeds the desired  $d_d$  within almost 0.5 h, while  $T_i$  and  $D$  are still undergoing their initial transients, see Fig. 10b and d. Despite fast processing, this is an undesirable situation in BM because of poor control of  $d$ , as shown by  $d_d$  being overshoot by 20% over the last transient sampling step  $t_{\text{sam}} = 5$  min. This is also highly undesirable because of the large disparity of processing time required to obtain the desired bilayer thickness  $b_d$  (Fig. 6) and desired penetration depth  $d_d$  (Fig. 10). For fixed power  $P$ , the total time  $Dt_{d0}$  needed for diffusion to penetrate from an initial depth  $d_0$  to the specified  $d_d$  can be obtained from the definition of  $d(t)$  in Eq. (16) as

$$Dt_{d0} = \frac{1}{4D} (d_d^2 - d_0^2) \quad (22)$$

This result should be compared with Fig. 10a and b as well as with Eq. (10).

## 4. Multivariable control implementation

### 4.1. Real-time model

As previously discussed, closed-loop control of bilayer thickness and penetration depth rely upon in-process feedback of their measurements, along with measurements of the two temperature states. However, non-destructive, non-invasive sensing of these variables is usually not practical during BM because of the rotating enclosed containers. Therefore, a process observer, i.e. a computational simulation of the BM process running in real-time and in parallel to the actual setup, should be used to provide state estimation. Despite their simplicity, the dynamic



ters. Therefore, this observation motivates the need for a more robust and comprehensive observer.

A real-time computational model (“RT Model”) for prediction of the evolving BM particulate structure, including microstructure geometry, material composition, and thermal exposure, has been recently demonstrated and reported elsewhere [16]. Synoptically, the RT Model follows the evolution of a single representative composite particulate as it is processed from similar clusters and deforming particles originating from the initial monometallic powders, modeled via warped ellipsoid domains, see Fig. 2. For a power input  $P$  to the BM device, the RT Model describes the impactor kinematics via a Maxwell–Boltzmann PDF of velocities  $v$  [18]. Upon an impactor-particulate collision simulated in a Lagrangian frame, the RT Model determines the impact energy  $U$  and the surface contact conditions, including the loading and ideal elastic deformations. By recasting this ideal impact energy to the elasto-plastic strain-hardening constitutive behavior of the materials (similarly to what discussed in Fig. 3a), the RT Model determines equivalent von Mises yield and Coulomb dry friction conditions. On this basis, volumetric plastic deformation is computed via Castigliano’s strain work theory, along surface friction slip resulting in heat dissipation and the formation or rupture of micro-welded joints among the particulate domains [16]. The predicted 2D dynamic microstructure of the particulate section is employed to derive average 3D bilayer thickness  $b$ , as for example in Fig. 11. At the same time, the dissipated heat by conduction in the particulate is used as a source for the temperature distribution, which is determined employing a Green’s function formalism [13,15], and successively employed to identify temperature-dependent material properties. These properties enable modeling of concentration profiles and diffusion penetration at bimetallic domain contacts [14]. This computationally efficient RT Model implemented on an ordinary computer (180 GIPS) can follow the BM process up to several hours, providing predictions of all necessary state variables at real-time observation speed [16].

## 4.2. Experimental validation

The computational model is validated via a laboratory device (“BM Setup”) for low-energy planetary BM (Fritsch Pulverisette, see [4]), with  $n = 5$  balls of diameter 10 mm in a  $w = 80$  ml cylindrical vial made of stainless steel in  $N_2$  inert atmosphere. Ni and Al powders (Alfa Aesar) are used in the tests, with mesh size  $-325$  ( $40 \pm 4 \mu\text{m}$ ), molar ratio 1:1 and total mass  $m_{\text{Ni}} + m_{\text{Al}} = 32$  g. The plastic deformation, thermal and diffusion parameter values for this setup are as previously reported. The device has been augmented for real-time sensing of external temperature  $T_o$  on the cylindrical walls of the rotating vials, see Fig. (7), by a stationary infrared thermocouple (Omega) inside the enclosure [13]. Matching of the predictions for  $T_o$  by the thermal description of Eq. (12) to the temperature measurements enables calibration of the initial BM efficiency parameter  $\eta$  in Eq. (5).

Fig. 11a–c shows the scanning electron microscopy (SEM) micrographs of Ni (bright phase)-Al (dark phase) particulates ball milled at 300 rpm for  $Dt_o = 5, 7$  and 10 h respectively, compared with the respective simulations of the real-time model under the same conditions in Fig. 11d–f. The structural geometry is illustrated to gradually transform from a globular agglomerate to a lamellar multilayer network with increasing fractal dimension  $F$  as BM progresses. These 2D microstructures are used to derive the average bilayer thickness values  $b$  and the rates of compression strain  $\dot{\epsilon}$  used in Fig. 4, thus validating the bilayer size dynamical models. For these test conditions, the RT Model also provides estimates of the internal temperature  $T_i$  in the BM vials (Fig. 10c) along with the average penetration depth  $d$  (Fig. 10a), also confirming the temperature and diffusion dynamical models. The predictions by the RT Model for diffusion penetration and material composition at the initiation of formation of intermetallic compounds (NiAl) are also corroborated against experimental X-ray diffraction (XRD) spectra of the particulates, both confirming nickel aluminide inception after nearly 13 h, see [4]. This onset of intermetallics formation corresponds to a critical cumulative diffused saturation mass  $\mathcal{Q}$ , which is in turn used to define the limit of penetration depth  $d_d$  in Eq. (16).

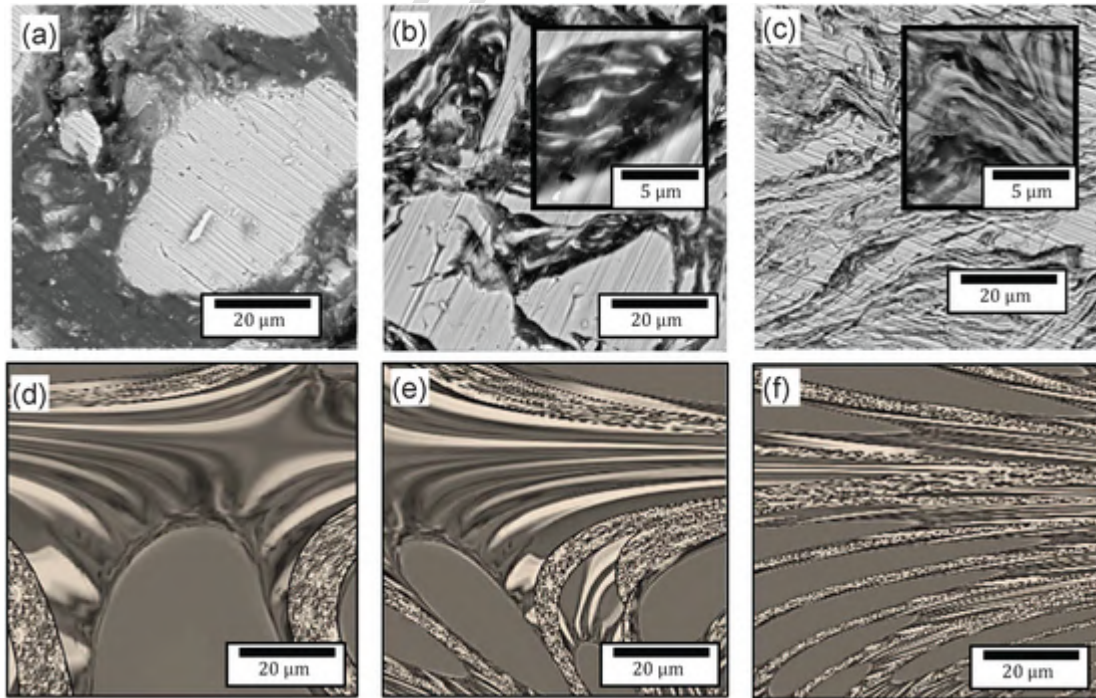


**Fig. 11.** Ni–Al particulate microstructure after BM with duration  $Dt_o$ , yielding average bilayer thickness  $b$  and fractal dimension  $F$ : (a), (b), (c) Experimental SEM micrographs [4]; (d), (e), (f) respective simulations of real-time model. (a)  $Dt_o = 5$  h,  $b = 13.2 \mu\text{m}$  ( $F = 2.498$ ). (b)  $Dt_o = 7$  h,  $b = 7.3 \mu\text{m}$  ( $F = 2.58$ ). (c)  $Dt_o = 10$  h,  $b = 2.6 \mu\text{m}$  ( $F = 2.716$ ). (d)  $Dt_o = 5$  h,  $b = 11.7 \mu\text{m}$  ( $F = 2.516$ ). (e)  $Dt_o = 7$  h,  $b = 6.7 \mu\text{m}$  ( $F = 2.62$ ). (f)  $Dt_o = 10$  h,  $b = 3.1 \mu\text{m}$  ( $F = 2.685$ ).

To maintain the faithfulness of the real-time computational model as an observer to the laboratory BM process, the energy efficiency parameter  $\eta$  needs to be identified and adjusted during operation. Such an adaptation law at steady state aims to reconcile the difference  $E_o$  between the actual infrared (IR) measurements  $T_o^*$  of the external vial temperature on the BM setup and the predictions  $T_o$  of the model (corresponding to output  $\theta_o$  in Eq. (12)), by changing the efficiency rate proportionally to the error (similarly to the so-called ‘‘MIT rule’’ [24,25]) so that  $\dot{\eta} = gE_o$ , where  $E_o = T_o^* - T_o$  and the adaptation gain is  $g = 10^{-3}/\text{K s}$ . This yields

$$\eta(t) = \eta(0) + g \int_0^t E_o(\tau) d\tau \quad (23)$$

This adaptation loop is also run at a period  $t_{\text{sam}} = 5$  min and is illustrated in Fig. 12, along with the control law discussed below.

### 4.3. Multivariable control

Simultaneous feedback control of the two primary BM outputs, average bilayer thickness  $b$  and diffusion penetration  $d$ , to specified values  $b_d$  and  $d_d$ , respectively, is achieved by modulating the process input, i.e. the device power  $P$ , in a single-input, multiple-output (SIMO) system shown in Fig. 12. Further, because of the nature of BM, it is preferable that the input  $P$  schedule consists of steady power segments (for example, as in Figs. 6a and 10c, minimizing accelerations of the BM containers and thermo-kinetic transients of their contents, thus maximizing process efficiency).

For steady state processing segments, from Eq. (10), since at thermal steady state  $\dot{\theta}_i = 0$ , the internal temperature is  $T_i = (r + R)\eta P + T_a$ . The required times  $Dt_b$  and  $Dt_d$  to obtain the desired  $b_d$  and  $d_d$  from  $b$  and  $d$  are thus, from Eqs. (10) and (22),

$$\begin{cases} Dt_b = \frac{1}{KP} \ln(b/b_d) \\ Dt_d = \frac{d_d^2 - d^2}{4D_0} \exp(Q_0 / [R((r + R)\eta P + T_a)]) \end{cases} \quad (24)$$

which clearly display the different effect of the power  $P$  on the processing times for the two principal BM outputs. Fig. 13 illustrates the relative rates at which the two phenomena progress depending on the power schedule, for representative initial conditions  $b_0 = 40 \mu\text{m}$  and

$d_0 = 0$  nm. At low  $P$  level, and hence lower  $T_i$ , plastic deformation leads over extremely slow diffusion, while at higher  $P$ , corresponding to elevated  $T_i$ , rampant diffusion dominates. Therefore, the different sensitivity of  $b$  and  $d$  on  $P$ , as determined in Eqs. (8) and (19), can be exploited in order to selectively grow each output through proper level and duration of steady input segments.

Because of the monotonically increasing accumulation of  $b$  and  $d$  over the BM process, a suitable real-time schedule of  $P$  should eventually obtain the reference  $b_d$  and  $d_d$  concurrently at the end of BM duration  $Dt$ . Thus, if at a certain process time  $t$ , the outputs  $b$  and  $d$  are available via estimates from the observer, then the required power level of a single steady input segment to lead the process to the specified set-points can be determined by equating  $Dt_b$  and  $Dt_d$  in Eq. (24). Specifically, letting  $Dt_b = Dt_d$  yields

$$P = \frac{4D_0 \ln(b/b_d)}{K(d_d^2 - d^2)} \exp\left[\frac{-Q_0/R}{(r + R)\eta P + T_a}\right] \quad (25)$$

which establishes an implicit inversion-type SIMO control law for  $P$ . Eq. (25) is solved for  $P$  by numerical fixed-point iterations (Picard algorithm [26]), i.e. by using the current  $P(i-1)$  value on the right hand side of Eq. (25) to obtain a first estimate of the new  $P(i)$  on the left hand side, and repeating for more accurate values in several iterations. A graphical interpretation of the method is displayed in Fig. 13. For example, the initial  $P(0)$  estimate for the given setup parameters (with  $\eta = 1$ ) and the previously discussed reference values ( $b_d = 2 \mu\text{m}$ ,  $d_d = 5$  nm) is determined at  $T_a = 288.3$  K, see Fig. 13.

## 5. Results and discussion

Fig. 14a and c shows the experimental responses of the closed-loop control system. After initial transient oscillations due to the adaptation of the efficiency parameter  $\eta$  from Eq. (23), the modulated power  $P$  from Eq. (25) with saturation at  $P_{\text{max}} = 300$  W settles to steady-state values, corresponding to the  $P_0$  value identified in Fig. 13. This yields steady-state temperatures  $T_i \approx 118.2$  °C and  $T_o = 114$  °C  $\approx T_o^*$ , consistent with the laboratory IR measurements, see Fig. 14c. When the BM process is completed and  $b = b_d$ , the control law of Eq. (25) shuts down the power to  $P = 0$  after a final transient oscillation. This input schedule within almost a single steady segment indeed achieves the specified output setpoints, see Fig. 14a, in approximately 13.5 h,

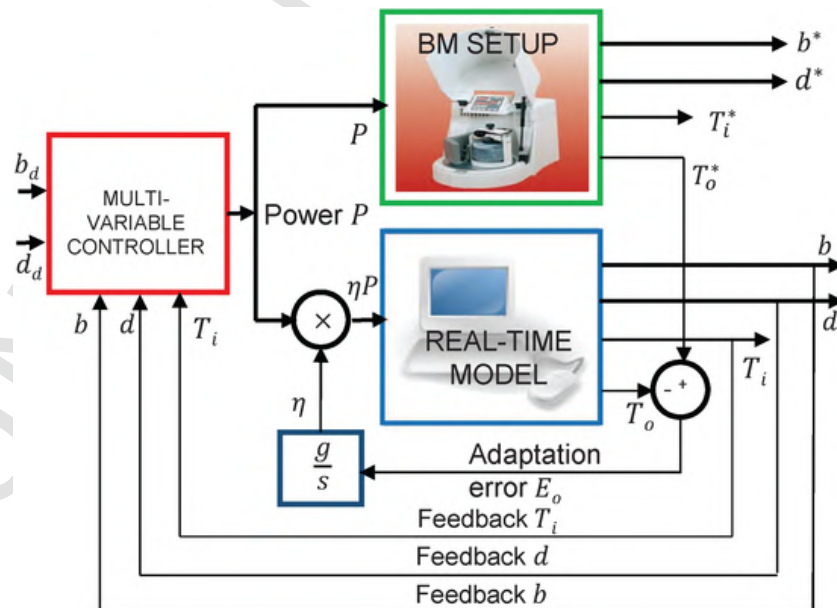


Fig. 12. Implementation of adaptive multivariable control for the BM Setup.

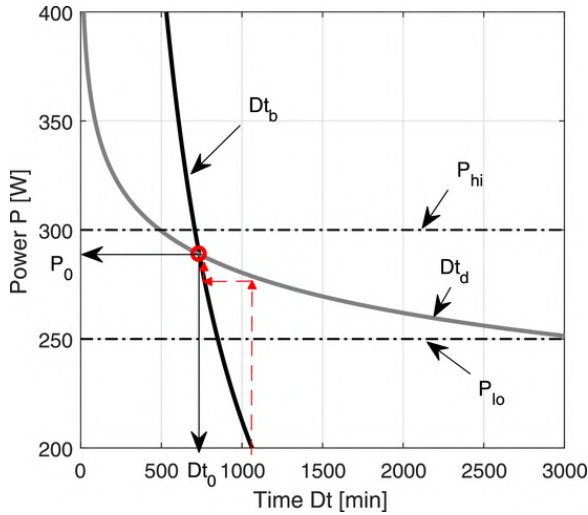


Fig. 13. BM time needed for plastic deformation  $Dt_{b0}$  and diffusion penetration  $Dt_{d0}$ , with  $b_0 = 40 \mu\text{m}$ ,  $d_0 = 0 \text{ nm}$ ,  $b_d = 2 \mu\text{m}$ , and  $d_d = 5 \text{ nm}$ . Dashed arrows indicate fixed-point iterations.

or approximately 1 h longer than expected in the determination of Fig. 13, where  $Dt_o = 740 \text{ min}$ . This discrepancy is due to inefficient transient periods.

Although nearly time-optimal, this power schedule may be undesirable for the BM device because of the bumpy transients and

noisy steady state variations. Thus, the previous control law can be modified to always saturate  $P$  at two fixed levels: a lower value  $P_{lo}$  (below  $P_0$  in Fig. 13, favoring plastic deformation) and a higher value  $P_{hi}$  (above  $P_0$ , favoring diffusion penetration). The two levels are switched when  $P$  crosses a threshold  $\Delta P$  around the mid-level  $P_{ave} = (P_{lo} + P_{hi})/2$

$$P = \begin{cases} P_{hi} & \text{if } P > P_{ave} + \Delta P \\ \text{Nochange} & \text{if } P_{ave} - \Delta P \leq P \leq P_{ave} + \Delta P \\ P_{lo} & \text{if } \Delta P < P < P_{ave} - \Delta P \\ 0 & \text{if } P \leq \Delta P \end{cases} \quad (26)$$

Fig. 14b and d shows the responses of the laboratory setup with the model observer under this control law, with  $P_{hi} = 300 \text{ W}$ ,  $P_{lo} = 250 \text{ W}$  and  $\Delta P = 15 \text{ W}$ . This controller produces an input schedule with two high-power ( $P_{hi}$ ) segments alternating with two low-power ( $P_{lo}$ ) segments, yielding respectively high and low levels of  $T_i$  and  $T_o$ , see Fig. 14b. The ensuing diffusivities  $D$  cause time intervals of faster and slower growth of the outputs  $b$  and  $d$  at proper rates to eventually reach the reference values. Thus, this system clearly achieves the control objective by modulation of the input duration. This control law avoids transient oscillations and steady state noise, at the expense of some extra processing time. In this example, approximately additional 0.5 h of processing are required ( $\approx 14 \text{ h}$  total BM time) because of the suboptimal  $P_{hi}$  and  $P_{lo}$  levels in comparison to  $P_0$ .

## 6. Conclusions and further research directions

In conclusion, the key finding of this article is that the microstructure and composition of ball-milled Ni and Al particulates can be simul-

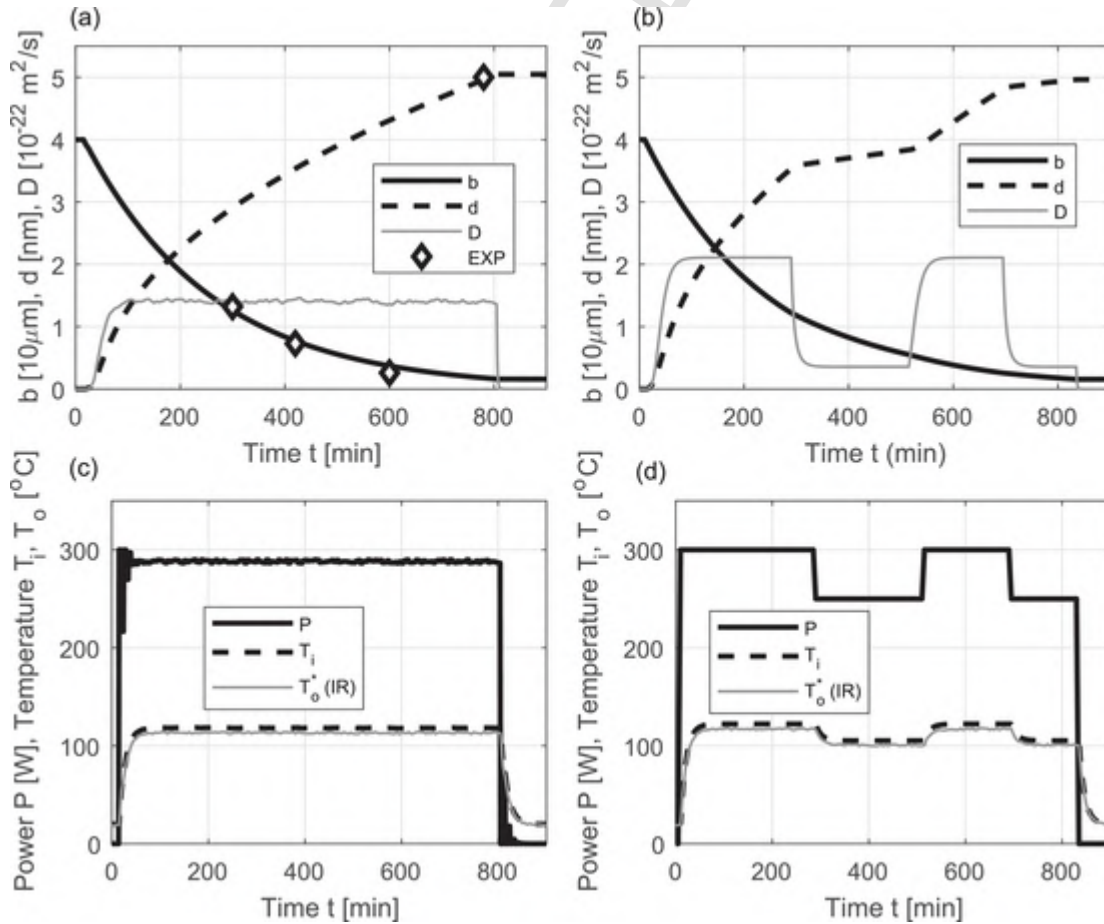


Fig. 14. Multivariable control and adaptation implementation with (a) and (c) variable  $P$ ; or (b) and (d) fixed  $P$  segments. (a) and (b) Responses of bilayer size  $b$ , penetration depth  $d$ , and diffusivity  $D$ . (c) and (d) Responses of power  $P$ , internal temperature  $T_i$  and external temperature  $T_o^*$  (as measured via IR). Data marked with EXP correspond to SEM/XRD experimental measurements.

taneously controlled, independently within certain limits, by properly modulating the BM power level during the process. This is because, during ball milling, the thickness of the Ni–Al bilayers, as they are formed by plastic deformation and surface friction, changes at a rate different from the rate of penetration depth of Ni into Al because of thermal diffusion. These two rates, determined chiefly by the material compressibility and thermal diffusivity, respectively, are ultimately dependent on the internal temperature in the vial for various BM power conditions. Thus, in principle, a high-power (and high-temperature) diffusive processing could yield the desired penetration of concentration; subsequently, a low-power (and low-temperature) deformation processing could bring the structural size to conform with a setpoint microstructure. Aside from developing a real-time computer control system to implement this strategy in the laboratory and in simulation, the chief contribution of this paper is in establishing the requisite analytical dynamic models of bilayer thickness and penetration depth through the coupled physics of deformation, friction, diffusion, and thermal transport.

More specifically, this work has introduced the theoretical framework and tested an experimental prototype of an effective multivariable feedback control scheme of BM plastic deformation and material diffusion effects. This control scheme employs a predictive computational model of particulate structure as a process observer, with real-time adaptation to the BM device through infrared measurements of external vial temperature. The presented research elucidates the different essential dependence of plastic deformation and diffusion penetration rates on the thermal state of BM materials. These in turn result from heat dissipation and heat transfer because of plastic yield and friction slip in the container vials.

Within the proposed control scheme, the intensity and duration of process power  $P$  cycles were modulated by the closed-loop controller in order to regulate internal temperature  $T_i$  and, consequently, material compressibility  $K$  and diffusivity  $D$ , so as to bring the bilayer thickness  $b$  and penetration depth  $d$  to specified reference sizes. Computational model estimates were calibrated via laboratory SEM and XRD data in processing of Ni and Al powders in a low-energy BM setup.

After elucidating the process-to-structure dependence and demonstrating simultaneous control of both its geometrical microstructure and material composition attributes, the structure-to-properties connection of the produced BM materials needs to be addressed, in order to establish the desired reference values of  $b_d$  and  $d_d$ . In addition to and beyond deformation of the bilayers and diffusion altering the material composition, future research directions are envisioned in modeling the in-process reaction phenomena in the bimetallic structures developing during ball milling. This is necessary as elevated internal temperatures and the variety of concentrations across the bilayers would yield a variety of nickel aluminide compositions in the Ni–Al phase diagram upon equilibrium. Thus, the kinetic rates of the respective solid solution reactions that could be activated under the energetic process conditions need to be assessed. As mentioned, such in-process partial reactions significantly reduce the chemical potentials and exothermic enthalpies of SPER upon ignition for use of the particulate product in its applications. This study is currently underway and is planned to be separately presented.

## Acknowledgements

This research was supported in part by a Khalifa University Internal Research Fund (Level 1) award.

**Conflict of interest:** None declared.

## References

- [1] T.P. Weihs, A.J. Gavens, M.E. Reiss, D. van Heerden, A. Draffin, D. Stanfield Self-propagating exothermic reactions in nanoscale multilayer materials. Proceedings of 1997 TMS annual meeting, Orlando, FL; 1997. p. 75–86.
- [2] E.L. Dreizin Metal-based reactive nanomaterials. *Prog Energy Combust Sci* 2009;35(2):141–167.
- [3] A.S. Rogachev, A.S. Mukasyan Combustion synthesis of materials: introduction to structural microkinetics. CRC Press; 2013.
- [4] A. Hadjiafrenti, I.E. Gunduz, C. Tsotsos, T. Kyratsi, C.C. Doumanidis, C. Rebolz Synthesis of reactive Al/Ni structures by ball milling. *Intermetallics* 2010;18(11):2219–2223.
- [5] O.S. Rabinovich, P.S. Grinchuk, M.A. Andreev, B.B. Khina Conditions for combustion synthesis in nanosized Ni/Al films on a substrate. *Physica B: Condens Matter* 2007;392(1–2):272–280.
- [6] E.M. Hunt, S. Malcolm, M.L. Pantoya, F. Davis Impact ignition of nano and micron composite energetic materials. *Int J Impact Eng* 2009;36(6):842–846.
- [7] D. Spitzer, M. Comet, C. Baras, V. Pichot, N. Piazzon Energetic nano-materials: opportunities for enhanced performances. *J Phys Chem Solids* 2010;71(2):100–108.
- [8] A.J. Gavens, D. Van Heerden, A.B. Mann, M.E. Reiss, T.P. Weihs Effect of intermixing on self-propagating exothermic reactions in Al/Ni nanolaminate foils. *J Appl Phys* 2000;87(3):1255–1263.
- [9] K. Falconer Fractal geometry. Wiley; 2013.
- [10] M. Ramasamy, S.S. Narayanan, C.D.P. Rao Control of ball mill grinding circuit using model predictive control scheme. *J Process Control* 2005;15(3):273–283.
- [11] X.S. Chen, J.Y. Zhai, S.H. Li, Q. Li Application of model predictive control in ball mill grinding circuit. *Miner Eng* 2007;20(11):1099–1108.
- [12] M. Sakaki, M.S. Bafghi, J.V. Khaki, Q. Zhang, F. Saito Control of carbon loss during synthesis of WC powder through ball milling of WO<sub>3</sub>-C-2Al mixture. *J Alloys Comps* 2009;486(1–2):486–491.
- [13] M. Aureli, A.S.M. Alzaabi, A.G.S. Hussien, C.C. Doumanidis, S.M. Jaffar, I.E. Gunduz, et al Thermostructural observation and adaptive control of fractal structure in ball-milled materials. *Mater Des* 2018;160:772–782.
- [14] M. Aureli, C.C. Doumanidis, I.E. Gunduz, A.G.S. Hussien, Y. Liao, N. Kostoglou, et al Bimetallic diffusion modeling and temperature regulation during ball milling. *Mater Des* 2018;155:233–243.
- [15] M. Aureli, C.C. Doumanidis, I.E. Gunduz, A.G.S. Hussien, Y. Liao, S. Jaffar, et al Non-equilibrium microscale thermomechanical modeling of bimetallic particulate fractal structures during ball milling fabrication. *J Appl Phys* 2017;122:25118.
- [16] M. Aureli, C.C. Doumanidis, I.E. Gunduz, A.G.S. Hussien, Y. Liao, C. Rebolz, et al Mechanics and energetics modeling of ball-milled metal foil and particle structures. *Acta Mater* 2017;123:305–316.
- [17] L. Bretzner, T. Lindeberg Feature tracking with automatic selection of spatial scales. *Comput Vision Image Underst* 1998;71(3):385–392.
- [18] C.C. Doumanidis, H.A. Al Kaabi, A.S. Alzaabi, I.E. Gunduz, C. Rebolz, C.C. Doumanidis Brownian-like kinematics of ball milling for particulate structural modeling. *Powder Technol* 2016;301:1077–1084.
- [19] J. Forshaw, G. Smith Dynamics and relativity. John Wiley & Sons; 2014.
- [20] K.J. Åström, B. Wittenmark Computer-controlled systems: theory and design. 3rd ed. Upper Saddle River, NJ: Prentice-Hall; 1997.
- [21] S.Q. Xi, J.G. Zhou, X.T. Wang Research on temperature rise of powder during high energy ball milling. *Powder Metall.* 2007;50(4):367–373.
- [22] V.P. Ramunni Diffusion behavior in nickel-aluminum and aluminum-uranium diluted alloys. *Comput Mater Sci* 2014;93:112–124.
- [23] M. Abramowitz, I.A. Stegun Handbook of mathematical functions: with formulas, graphs, and mathematical tables. New York: Dover Publications, Inc.; 1972.
- [24] K.J. Åström, B. Wittenmark Adaptive control. Addison-Wesley; 1995.
- [25] C. Adrian, A. Corneliu, B. Mircea The simulation of the adaptive systems using the mit rule. Proceedings of the 10th WSEAS international conference on mathematical methods and computational techniques in electrical engineering, Sofia, Bulgaria; 2008. p. 301–305.
- [26] S.C. Chapra, R.P. Canale Numerical methods for engineers. 4th ed. McGraw-Hill; 2002.